Forward Modeling of Active Region Coronal Emissions. II. Implications for Coronal Heating

2008 ApJ 689 1388

(http://iopscience.iop.org/0004-637X/689/2/1388)

The Astrophysical Journal, 689:1388–1405, 2008 December 20

FORWARD MODELING OF ACTIVE REGION CORONAL EMISSIONS. II. IMPLICATIONS FOR CORONAL HEATING

L. L. Lundquist[1,2]
Harvard-Smithsonian Center for Astrophysics, 60 Garden Street MS-58, Cambridge, MA 02138; llundquist@cfa.harvard.edu

G. H. Fisher
Space Sciences Laboratory, University of California, Berkeley, CA 94720-7450

T. R. Metcalf and K. D. Leka
Northwest Research Associates, Colorado Research Associates Division, 3380 Mitchell Lane, Boulder, CO 80301

and

J. M. McTiernan
Space Sciences Laboratory, University of California, Berkeley, CA 94720-7450
Received 2007 April 8; accepted 2008 March 31

ABSTRACT

In Paper I, we introduced and tested a method for predicting solar active region coronal emissions using magnetic field measurements and a chosen heating relationship. Here, we apply this forward-modeling technique to 10 active regions observed with the Mees Solar Observatory Imaging Vector Magnetograph and the *Yohkoh* Soft X-ray Telescope. We produce synthetic images of each region using four parameterized heating relationships depending on magnetic field strength and geometry. We find a volumetric coronal heating rate (dE_H/dV, not to be confused with dE_H/dA quoted by some authors) proportional to magnetic field and inversely proportional to field-line loop length (BL^{-1}) best matches observed coronal emission morphologies. This parameterization is most similar to the steady-state scaling of two proposed heating mechanisms: van Ballegooijen's "current layers" theory, taken in the AC limit, and Parker's "critical angle" mechanism, in the case where the angle of misalignment is a twist angle. Although this parameterization best matches the observations, it does not match well enough to make a definitive statement as to the nature of coronal heating. Instead, we conclude that (1) the technique requires better magnetic field measurement and extrapolation techniques than currently available, and (2) forward-modeling methods that incorporate properties of transiently heated loops are necessary to make a more conclusive statement about coronal heating mechanisms.

Subject headings: Sun: corona — Sun: magnetic fields — Sun: X-rays, gamma rays

Online material: extended and color figures

1. INTRODUCTION

The energy flux needed to maintain the large temperature imbalance between the hot active region corona and the much cooler photosphere is of the order of 10^7 erg cm^{-2} s^{-1} (Withbroe & Noyes 1977). Various authors over several decades have proposed heating mechanisms as the source of this energy flux. For reviews of proposed heating mechanisms and observational tests, see Gomez (1990), Zirker (1993), Narain & Ulmschneider (1996), Fisher et al. (1998), Mandrini et al. (2000), Walsh & Ireland (2003), Aschwanden (2004), and Klimchuk (2006).

Most theories that have proven plausible identify motions of the filamented magnetic field in the photosphere and convection zone as the energy source. These subatmospheric motions do work on the coronal magnetic field by displacing the footpoints of the magnetic field that occupies the corona but is rooted far below the photosphere. The source of controversy stems from the mechanism through which this energy is released as heat into the corona. Because of the very small values of classical dissipation coefficients in the corona, very steep gradients in either magnetic field and/or velocities are required to produce significant heating. Thus, modern day and currently anticipated observing instruments are not able to observe at the small spatial scales on which these heating processes operate. Instead, we are forced to rely on indirect effects of the heating mechanism on the overall plasma environment. Observational work has focused on these indirect effects and differences between the predicted large-scale effects of different heating mechanisms.

For example, one can examine correlations ("scaling relationships") between heating rates and physical observables such as field strengths, length scales, and velocities. These scaling relationships can be inferred from observations and derived from theoretical heating mechanisms. Comparison between the two yields observational constraints on the set of plausible heating theories, enabling rejection of potential heating mechanisms by process of elimination.

This approach has been applied by a number of authors. Klimchuk & Porter (1995) and Porter & Klimchuk (1995) examined scaling relationships for individual coronal loops, finding that volumetric heating rate scales inversely with length to the second power ($E_H \propto L^{-2}$), assuming steady heating with loops in quasi-static equilibrium. Mandrini et al. (2000) try to determine a relation between magnetic field and loop length in order to use this result to rule out potential heating mechanisms. They find that for loops such as those in the Klimchuk & Porter (1995) study, the average magnetic field scales inversely with length to a power of 0.88 ($\bar{B} \propto L^{-0.88}$) in a variety of potential, linear force-free, and magnetostatic coronal magnetic field extrapolations. They

[1] Space Sciences Laboratory, University of California, Berkeley, CA 94720-7450.
[2] The Institute of Space and Astronautical Science, Sagamihara 229, Japan.

find that most of the 22 different heating theories they examine fall within the error range of the Klimchuk & Porter (1995) results. They did, however, note an observational distinction between "stressing" or "direct current (DC)" models, where footpoint motions are slow enough for quasi-static evolution, and "wave" or "alternating current (AC)" models, where footpoint motions are faster than the Alfvén transit times of coronal loops. They find that DC models overall have better agreement with the Klimchuk & Porter (1995) results, and the worst agreement is for wave heating models that have a power spectrum in frequency imposed at the boundary.

However, these results applied only to relatively long, distinct, and easily observed active region loops with long lifetimes, such as the 47 loops selected for the study. It is not clear that these results should generalize to other loops. Ofman et al. (1996), for example, found a different relationship for loop transient brightenings: $E_H \propto L^{0.6}$.

Other authors have applied the approach to larger regions to avoid these inherent selection effects. Golub et al. (1980) used *Skylab* to find a relationship between observed pressures, magnetic field strength, and active region size. Other authors who have investigated observed active region scaling relationships include Falconer (1997), who examine relationships between neutral-line length and total brightness; Fisher et al. (1998), who study correlation between luminosity, magnetic flux, and electric current; Yashiro & Shibata (2001), who examine relations between temperature and pressure and active region size; and Démoulin et al. (2003), who extend the Mandrini et al. (2000) study to the active region level and examine the relationship between heating and density. Scaling studies have also been performed on nonactive region features; these include Pevtsov et al. (2003), who extend the Fisher et al. (1998) study to include quiet Sun features, X-ray bright points, full disk solar integrations, and other stars; Schrijver & Aschwanden (2002), who also consider scaling relationships on other stars; and Foley et al. (2002), who study coronal streamers.

Two weaknesses of the above studies include (1) the uncertainty inherent in the inversion techniques used to obtain many of the observables, and (2) a trade-off between either broad averaging over large spatial scales (as when the properties of an entire active region are reduced to a single quantity) or selection effects and line-of-sight integration (in the case of individual loop studies). Studies that rely on temperature or emission measure measurements generally use either a filter-ratio technique or spectrograph data that are of relatively low spatial resolution. The filter-ratio technique has a number of well-known flaws, particularly for narrowband imagers (e.g., Reale & Peres 2000; Martens et al. 2002; Schmelz et al. 2003; Weber et al. 2005), and both methods can yield only values that are weighted averages along the line of sight (see, e.g., Klimchuk & Cargill 2001).

One way to make progress beyond these limitations is to use these same scaling laws with forward-modeling techniques. This approach involves modeling coronal emissions using a parameterized scale-law form of the coronal heating mechanism to predict the magnitude and spatial distribution of emissions from a given active region and compare with observed emissions. Scaling relationships that better predict the observations are more likely to represent the true coronal heating mechanism. (A preferable approach would be to model heating mechanisms directly, rather than using the crude scaling-law approach, but at this time, models able to simulate both the small-scale, dynamic heating mechanism and the large-scale plasma response remain computationally prohibitive.)

The forward-modeling scaling-law approach has been applied by a few authors. Schrijver et al. (2004) used a potential field source-surface model and one-dimensional (1D) static energy solutions to synthesize full-Sun visualizations on two case study dates. Lundquist et al. (2004) and Warren & Winebarger (2006) expand on the technique of Schrijver et al., using a more realistic 1D steady-state loop model, and Warren & Winebarger (2007) go further by employing a dynamic loop model. Mok et al. (2005) use the most sophisticated technique with a 3D MHD model.

The degree of computational sophistication involves tradeoffs in the accuracy of the modes versus the number of computations permitted and the parameter space that can be explored. Schrijver et al.'s analytic, semicircular approximations to a static loop model from Aschwanden & Schrijver (2002) allow them to model 50,000 loops across the Sun and explore a large number of heating scale relationships (225 different parameterizations). However, the approximation in their energy calculation treats individual loop legs separately, such that loops have discontinuities in pressure and temperature at their apex. At the other end of the spectrum, Mok et al. (2005) treat the problem in the full three dimensions, beginning with a linear force-free magnetic field calculation, followed by an energy balance calculation along a static magnetic field. Their MHD model (with a low-β approximation) is able to perform a more realistic calculation of energy balance in the corona than a number of existing MHD models, as it includes thermal conduction along the magnetic field. Thus they can model full 3D emissions, unconstrained by field-line representations or interpolation difficulties. However, the computational time required to resolve the transition region in their model is still prohibitively large, which can have a significant effect on plasma emissions. Even without the transition region, the computational time required for a 3D calculation prevents large explorations of parameter space.

In this paper, we take an intermediate approach to achieve relatively accurate magnetic field and energy calculations while limiting computational expense. Our method is laid out in full detail in Lundquist et al. (2008, hereafter Paper I). We employ a more sophisticated nonlinear (nonconstant α) force-free field solution than any of the above studies. This model is particularly appropriate when dealing with active regions that are less likely to be potential. Our steady-state loop solutions are more sophisticated than those in the Schrijver et al. (2004) approach (as they include steady-state flows, giving us loops without discontinuities), similar to those of Warren & Winebarger (2006), and less sophisticated than the dynamic model of Warren & Winebarger (2007). The 1D approach is less rigorous than the 3D approach employed by Mok et al. (2005), but it does enable us to adequately resolve the transition region. These compromises place our computational time in the intermediate realm of these previous studies and enables us to perform a modest number of heating parameterizations (4) for a modest number of active region case studies (10).

We compute synthetic images of the predicted coronal magnetic emission for 10 different active regions of a variety of sizes and types, for which vector magnetogram data is available. We compare the synthetic images with observations from the *Yohkoh* Soft X-ray Telescope (SXT). Section 2 presents the scaling relationships predicted by different coronal heating models and their relation to the four parameterizations of the heating term employed in this model. Sections 3.1 through 3.5 present results from our best-reproduced active region, AR 8891, and discuss a number of issues involved in interpreting the figures and tables for each of the other active regions. The other nine regions are presented in

TABLE 1
Heating Scale Relationships

Description	Number	Reference	MDK Scaling	B Case a	B Case b	B Case c	L	L Range
Stochastic buildup	1	1	$B^2L^{-2}V^2\tau$	B^2	B^1	B^2	L^{-2}	...
Critical angle	2	2	$B^2L^{-1}V^1\tan\theta$	B^2	$B^{1.5}$	B^2	L^{-1}	...
Critical twist	3	3	$B^2L^{-2}V^1R^1\phi$	B^2	B^1	...	L^{-2}	...
Reconnection $\propto v_A$	4	4	$B^1L^{-2}\rho^{0.5}V^2R^1$	B^1	...	$B^{0.5}$	$L^{-2.45}$	$[-2.63, -2.17]$
Reconnection $\propto v_{A\perp}$	5	5	$B^{1.5}L^{-1.5}\rho^{0.25}V^{1.5}R^{1.5}$	$B^{1.5}$	...	$B^{0.75}$	$L^{-1.725}$	$[-1.815, -1.585]$
Current layers (DC)	6	6	$B^2L^{-2}V^2\tau\log R_m$	B^2	...	...	L^{-2}	...
	7	7	$B^2L^{-2}V^2S^{0.1}\tau$	B^2	...	...	L^{-2}	...
	8	8	$B^2L^{-2}V^2\tau$	B^2	...	...	L^{-2}	...
Current sheets	9	9	$B^2L^{-1}R^{-1}V_{\rm ph}^2\tau$	B^2	...	$B^{2.5}$	L^{-1}	...
Taylor relaxation	10	10	$B^2L^{-2}V_{\rm ph}^2\tau$	B^2	...	...	L^{-2}	...
Turbulence (DC) with:								
Constant dissipation coefficients	11	11	$B^{1.5}L^{-1.5}\rho^{0.25}V^{1.5}R^{1.5}$	$B^{1.5}$	...	$B^{0.75}$	$L^{-1.725}$	$[-1.815, -1.585]$
Closure	12	12	$B^{1.67}L^{-1.33}\rho^{0.17}V^{1.33}R^{0.33}$	$B^{1.67}$	...	$B^{1.505}$	$L^{-1.483}$	$[-1.5442, -1.3878]$
Closure + spectrum ($s = 0.7$)	13	13	$B^{1.7}L^{-1.7}\rho^{0.15}V^{1.3}R^{0.7}$	$B^{1.7}$	...	$B^{1.35}$	$L^{-1.835}$	$[-1.889, -1.751]$
Closure + spectrum ($s = 1.1$)	14	13	$B^{2.1}L^{-2.1}\rho^{-0.05}V^{0.9}R^{1.1}$	$B^{2.1}$	...	$B^{1.55}$	$L^{-2.055}$	$[-2.037, -2.083]$
Resonance ($m = -1$)	15	14	B^0L^{-2}	B^0	...	...	L^{-2}	...
Resonance ($m = -2$)	16	14	$B^{-1}L^{-1}\rho^{0.5}$	B^{-1}	...	...	$L^{-1.45}$	$[-1.63, -1.17]$
Resonant absorption I ($m = -1$)	17	15	B^0L^0	B^0	...	...	L^0	...
Resonant absorption I ($m = -2$)	18	15	$B^{-1}L^1\rho^{0.5}$	B^{-1}	...	...	$L^{0.55}$	$[0.37, 0.83]$
Resonant absorption II ($m = -1$)	19	16	$B^0L^1\rho^1$	B^0	...	...	$L^{0.1}$	$[-0.26, 0.66]$
Resonant absorption II ($m = -2$)	20	16	$B^{-1}L^2\rho^{1.5}$	B^{-1}	...	...	$L^{0.65}$	$[0.11, 1.49]$
Current layers (AC)	21	17	$B^1L^{-1}\rho^{0.5}V^2$	B^1	...	...	$L^{-1.45}$	$[-1.63, -1.17]$
Turbulence (AC)	22	18	$B^{1.67}L^{-1.33}R^{0.33}$	$B^{1.67}$	...	$B^{1.505}$	$L^{-1.33}$	...

Notes.—Heating scale relationships for models in MDK. Also shows B scaling for three cases: (a) R and V independent of B; (b) $R \propto B^{-1/2}$ due to magnetic flux conservation, and $V \propto B^{-1/2}$ (relevant for twist-type velocities); (c) $R \propto B^{-1/2}$ and V independent of B (relevant for translation-type velocities). L scaling also shown, assuming $\rho \propto L^{\epsilon}$, with MDK observed value $\epsilon = -0.9$, plus the range of ϵ values from our model loops: $\epsilon \in [-0.34,\ 1.26]$.

References.—(1) Sturrock & Uchida 1981, Berger 1991; (2) Parker 1988, Berger 1993; (3), Galsgaard & Nordlund 1997; (4) Parker 1983; (5) Parker 1983, modified; (6) van Ballegooijen 1986; (7) Hendrix et al. 1996; (8) Galsgaard & Nordlund 1996; (9) Aly & Amari 1997; (10) Heyvaerts & Priest 1984, Browning & Priest 1986, Vekstein et al. 1993; (11) Einaudi et al. 1996, Dmitruk & Gomez 1997; (12) Heyvaerts & Priest 1992, Inverarity et al. 1995, Inverarity & Priest 1995a; (13) Milano et al. 1997; (14) Hollweg 1985; (15) Ofman et al. 1995; Ruderman et al. 1997; (16) Halberstadt & Goedbloed 1995; (17) Galsgaard & Nordlund 1996; (18) Inverarity & Priest 1995b. References, model numbers, and descriptions from MDK.

§ 3.6. We present conclusions, including discussion of the forward model's accuracy in reconstructing coronal emissions and its implications for coronal heating constraints, in § 4.

2. SCALING RELATIONSHIPS

Table 1 shows the scaling relationships for the 22 different coronal heating theories presented in Mandrini et al. (2000, hereafter MDK). These scaling laws are determined through consideration of the rate at which a net energy is pumped into the corona via magnetic footpoint motions that either stress the coronal magnetic field (DC models) or inject waves into the corona (AC models). The energy is eventually dissipated as heat, although the details of a specific dissipation mechanism are not needed to derive a scaling relationship. Each theory predicts a level of heating that scales with parameters such as the magnetic field B, loop length L, plasma mass density ρ, coronal loop velocity V, angle between adjacent coronal loops θ, twist angle of coronal loop ϕ, timescale τ, magnetic Reynolds number R_m, and Lundquist number S. In some cases, these parameters do not have a completely straightforward interpretation, as MDK point out. We treat L as the loop length in each case, but in some models (9, 10, 12, and 22), it is more properly interpreted as the characteristic width of an assumed magnetic arcade. We refer the reader to MDK for a more in-depth description of parameters as they relate to each theory; here we concern ourselves only with the relative scaling with B and L.

We assume, like MDK, that the parameters τ, θ, ϕ, R_m, and S are independent of B and L. The parameters R, V, and ρ are not as straightforward.

R, in most instances, is the radius of a coronal loop's cross section. Assuming magnetic flux conservation, the cross sectional loop area would vary inversely with magnetic field strength. This implies $R \propto B^{-1/2}$. However, to the limit of instrument resolution, coronal loops are observed to have relatively constant loop radii (Klimchuk et al. 1992, 2000; Watko & Klimchuk 2000; Lopez Fuentes et al. 2006). Furthermore, the parameter R may not always be interpreted as strictly equal to the loop radius. In some cases it is more properly interpreted as a characteristic horizontal lengthscale for the magnetic field and/or flow field. Thus, we consider two cases, one where $R \propto B^{-1/2}$ and one where R is independent of B.

Similarly, the scaling of R can affect the scaling of V, the loop velocity, which sometimes represents a twisting velocity and other times represents a translational velocity of the loop footpoints. For the case of twisting velocities, with $R \propto B^{-1/2}$, we will also have $V \propto B^{-1/2}$. Some of the models permit only a twist-type velocity interpretation, while others permit only a translation-type velocity interpretation. Still others may be interpreted in either way.

The combination of possible interpretations for the parameters R and V gives us a total of three different cases for B scaling. Case (a) assumes that R and V are independent of B. Case (b) assumes that $R \propto B^{-1/2}$ and $V \propto B^{-1/2}$, a formulation relevant for twisting-type velocities. Case (c) assumes $R \propto B^{-1/2}$ but V is independent of B, a formulation relevant for translation-type velocities. Cases (a) and (b) mirror the two cases considered in MDK.

The mass density ρ has been shown observationally to be related to loop length, $\rho \propto L^{\epsilon}$. MDK find a value of $\epsilon = -0.9$ through a reanalysis of the results of Porter & Klimchuk (1995). We have assumed this value to determine the overall L scaling of each heating mechanism, and the results are listed in Table 1. After completing each coronal loop solution (§ 2.2 of Paper I),

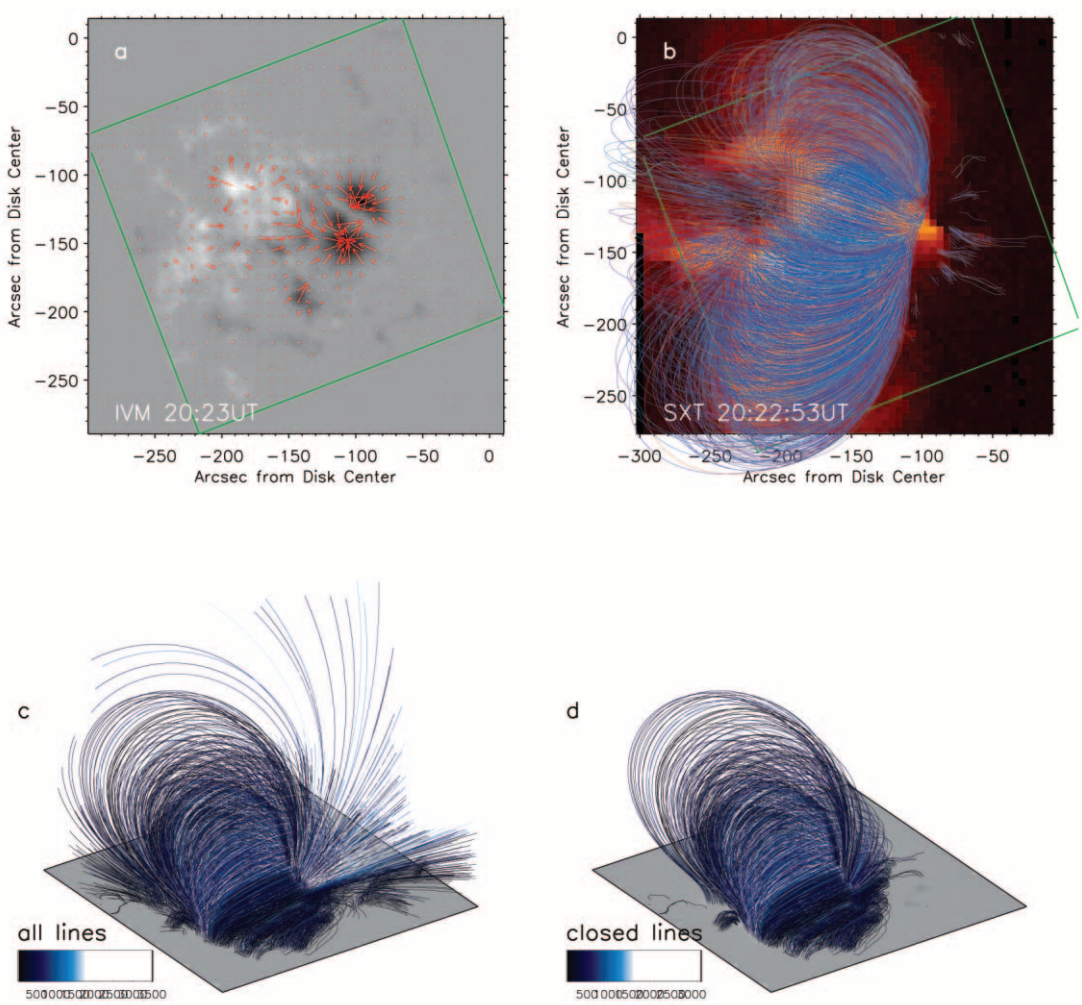

FIG. 1.—Magnetic field for AR 8891, showing (*a*) vector magnetogram data, (*b*) field lines plotted over SXT observations, (*c*) all force-free field solution field lines, and (*d*) closed field lines used in synthetic image calculations. [*See the electronic edition of the Journal for a color version of this figure.*]

we analyzed the results to see if the theoretical loops predict the same scaling. We find a value of ϵ that varies between -0.34 and -1.26, depending on which active region and which heating parameterization is employed. We show how this range of values affects the L scaling for each heating mechanism in the final column of Table 1. Because we find a value of ϵ that varies for different coronal heating mechanisms, we must check for self-consistency after the modeling is accomplished to determine if the scaling of ρ with L assumed in the heating mechanism matches the scaling exhibited in the loop calculations. We return to this issue in § 4.2.

3. RESULTS

Based on the range of theoretically proposed scalings of coronal heating with B and L outlined in the previous section, we select four representative scaling relationships to test in the forward model: B/L, B/L^2, B^2/L, and B^2/L^2. (We emphasize that these relationships express volumetric heating rates, as opposed to the expressions of heat flux density used in Schrijver et al. 2004. Section 4.2 describes how to compare our results with those of that paper.) In this section, we present results from 10 case study active regions.

For each active region (except 8210, which was shown in Paper I), we show four images that illustrate the magnetic field data, the coronal magnetic field solution, the field lines we model as coronal loops, and their relation to the emission as observed with the *Yohkoh* Soft X-ray Telescope (SXT) at a time close to the magnetogram observations. We also show six images illustrating the observed and predicted coronal emissions: the four synthetic images created with four different heating parameterization assumptions, plus the observed SXT emissions for comparison, in full-Sun view and cropped identically to the synthetic emission calculated inside the force-free solution box. These images comprise Figures 1–10. (Only a subset of the figure subparts are available in the print edition; the rest are available in the online edition of this paper.)

In §§ 3.1–3.5, we use results from AR 8891 to illustrate some common features shared for all the active regions, and to point out important subtleties for interpreting the data presented. Because some features of the images are quite confusing, we address some of these issues in a question-and-answer style format.

3.1. *Magnetogram Data, as in Figure 1a*

Our technique for taking and processing vector magnetogram data is described in Paper I. Figure 1*a* shows the vector magnetogram data from AR 8891, embedded in the bottom boundary of the force-free-field solution box. The green line outlines the extent of the original data. Values outside this boundary are set to zero. The gray scale shows the longitudinal magnetic field, with white representing positive polarity and black representing negative polarity. Red arrows indicate the direction of the transverse field.

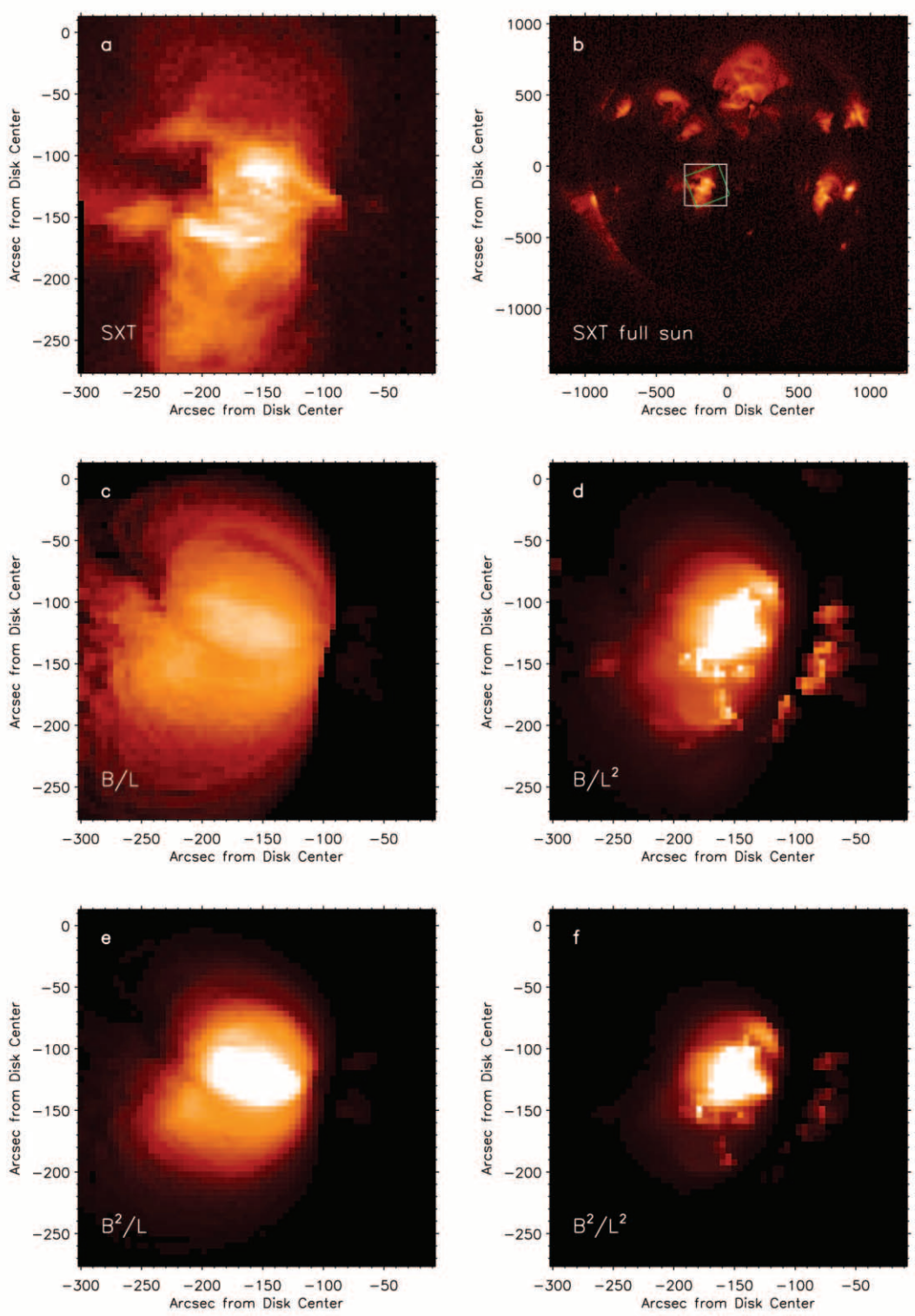

FIG. 2.—SXT observations of AR 8891 in (*a*) close-up and (*b*) full Sun views, compared with four synthetic images with heating relationships: (*c*) B/L, (*d*) B/L^2, (*e*) B^2/L, and (*f*) B^2/L^2. All have same color scaling. [*See the electronic edition of the Journal for a color version of this figure.*]

3.1.1. *Why are the Magnetogram Data Tilted with Respect to the Force-Free-Field Solution Box?*

The force-free-field solution code requires a bottom boundary in heliographic coordinates (at disk center), as opposed to image coordinates (normal to the plane of the sky, as viewed from Earth). This is because the longitudinal and transverse fields must be perpendicular to one another, with the transverse field parallel to the solution boundary, and the longitudinal field perpendicular to solar surface. Furthermore, both the IVM and SXT data are rotated to a zero solar *p*-angle[3] configuration, causing the IVM data to appear tilted, depending on the solar *p*-angle as viewed from Earth on the day of the magnetogram measurement. We take the force-free-field solution box to be the smallest rectangle

[3] The solar *p*-angle is the angle between the Sun's axis of rotation and the plane normal to the Earth-Sun line.

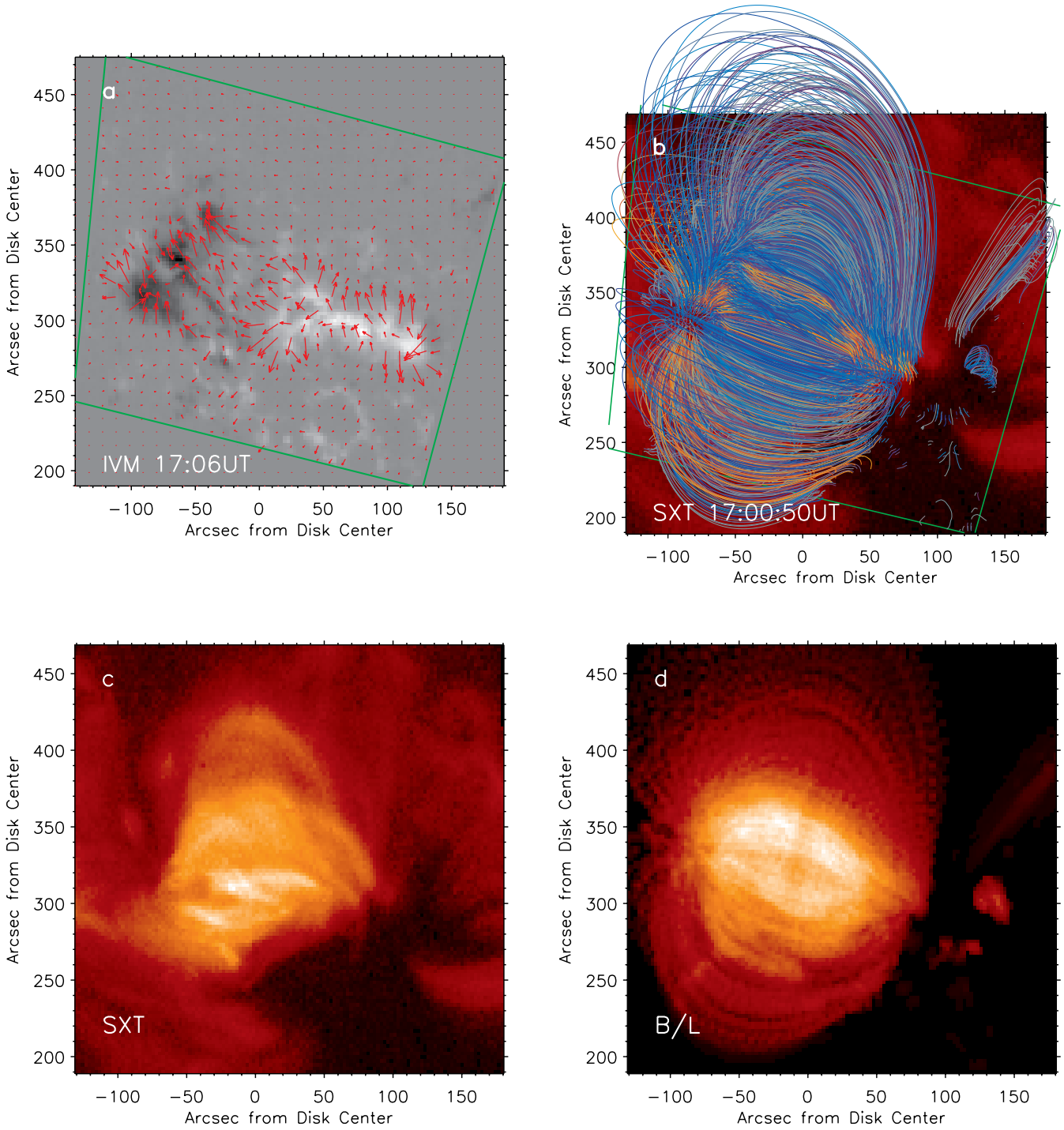

FIG. 3.—AR 8651, showing (*a*) vector magnetogram data, (*b*) field lines plotted over SXT observations, (*c*) SXT observations, and synthetic images for heating relationships (*d*) B/L, (*e*) B/L^2, (*f*) B^2/L, and (*g*) B^2/L^2. Also shown are (*h*) SXT observations in full Sun views, (*i*) all force-free field solution field lines, and (*j*) closed field lines used in synthetic image calculations. [*See the electronic edition of the Journal for a color version and panels e–j of this figure.*]

that encloses the IVM data in heliographic coordinates. We also rebin these data to a 128×128 grid to reduce the nonlinear force-free-field computation time (typically about 24 hr for one force-free-field extrapolation using the IDL version on a modern desktop machine).

3.1.2. *Why Does the Green Line Outlining the Magnetogram Data Sometimes Appear to be Nonrectangular* (*e.g., Fig. 10a*)*?*

This is also a result of the move from image coordinates to heliographic coordinates. Data far from disk center will be more warped than data near disk center. Also, there may be a small amount of warping that occurs during co-alignment. Before we transform the vector magnetogram data to heliospheric coordinates, we first co-align them with the MDI data to improve the data pointing information, as described in Paper I. The polynomial warping algorithm for feature-based co-alignment makes small adjustments to line up features from the IVM and MDI data. For most of the regions, we find that the alignment algorithm works better on the white-light data available from both IVM and MDI, but for a few of the small regions (AR 9659,

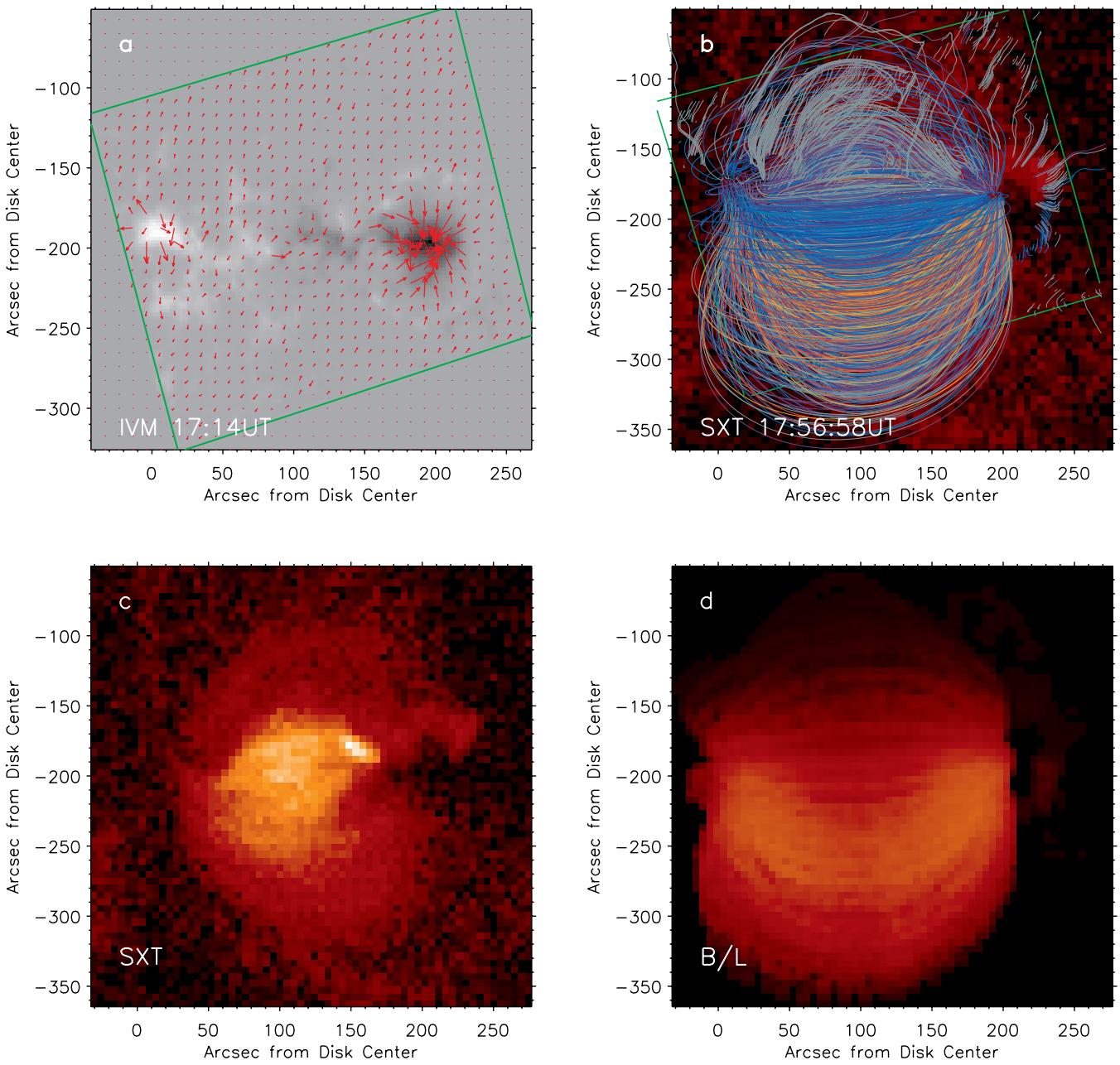

FIG. 4.—AR 9017, showing (*a*) vector magnetogram data, (*b*) field lines plotted over SXT observations, (*c*) SXT observations, and synthetic images for heating relationships (*d*) B/L, (*e*) B/L^2, (*f*) B^2/L, and (*g*) B^2/L^2. Also shown are (*h*) SXT observations in full Sun views, (*i*) all force-free field solution field lines, and (*j*) closed field lines used in synthetic image calculations. [*See the electronic edition of the Journal for a color version and panels e–j of this figure.*]

AR 9714, and AR 9731) where there are little or no apparent sunspot regions, we perform the alignment on the line-of-sight magnetic data.

3.2. *Alignment of Coronal Emissions and Magnetic Field Data, as in Figure 1b*

Figure 1*b* and subsequent similar figures show how field lines from the magnetic field solution compare to the coronal SXT emissions. The coronal emissions from a time near to the time of the magnetogram data are plotted, overlaid with the field lines from coronal magnetic field solution. Field-line color is based on magnetic field strength. (Note that the color table for the field lines in Fig. 1*b* is periodic, and is different from that in Figs. 1*c* and 1*d*, for the purpose of improved viewing on a dark background.) The green outlines from Figure 1*a* are repeated in Figure 1*b* to indicate the extent of the original magnetogram data.

3.2.1. *How is the Cropping of the Coronal Emissions Determined?*

When only full-Sun SXT emissions are available, we crop the emissions to the smallest box that encloses all of the closed field lines from the calculation. When higher resolution partial-field images are available from SXT (as for regions 8210, 8651, 8891, and 9026), we first create a synthetic image based on a box enclosing all field lines and then crop these synthetic emissions to the field of view of the observations. For these regions, some field lines extend beyond the bounds of the SXT observations, as seen in Figure 1. (Field lines are chosen as described in Paper I.)

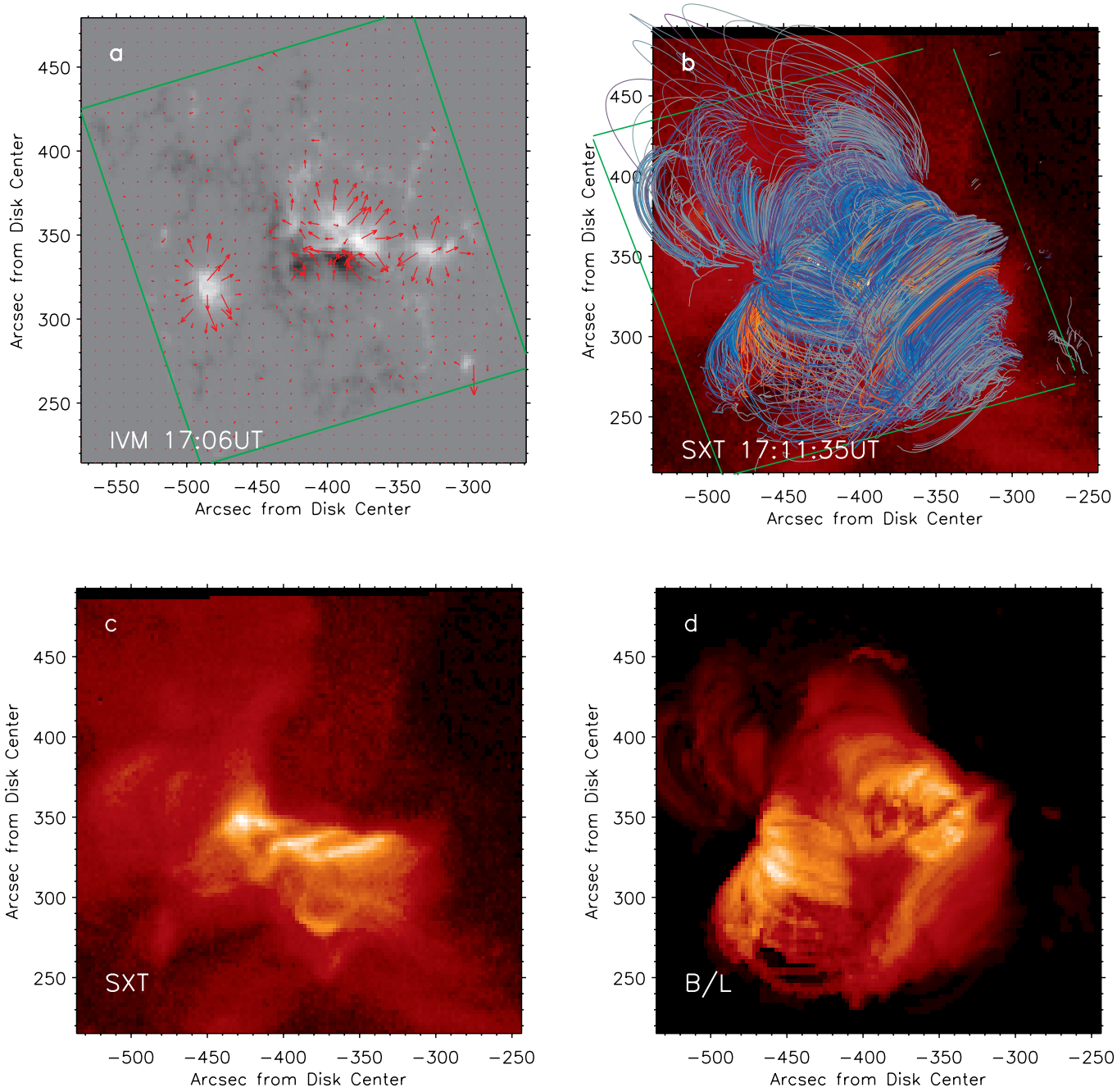

FIG. 5.—AR 9026, showing (*a*) vector magnetogram data, (*b*) field lines plotted over SXT observations, (*c*) SXT observations, and synthetic images for heating relationships (*d*) B/L, (*e*) B/L^2, (*f*) B^2/L, and (*g*) B^2/L^2. Also shown are (*h*) SXT observations in full Sun views, (*i*) all force-free field solution field lines, and (*j*) closed field lines used in synthetic image calculations. [*See the electronic edition of the Journal for a color version and panels e–j of this figure.*]

We first perform energy balance calculations along each of the field lines shown and interpolate the emissions onto a 3D grid (see Paper I). This grid is aligned such that the z-axis is parallel to the line of sight from the *Yohkoh* satellite to the Sun, with the x and y grid oriented to same angle, spacing, and location as the pixels of the SXT instrument. The synthetic emissions are calculated for the set of pixels that encloses all of the closed field lines. Where observations exist that fall outside the box, the observations are cropped. Where synthetic emissions exist that fall outside the observations, the synthetic emission images are cropped. For AR 8210 (discussed in Paper I), this means that the observations get cropped on the left-hand-side to the leftmost point where a closed field line exists, while the synthetic images get cropped on the right-hand side to the rightmost place where the SXT partial-field observations exist. For example, in Figure 11, the left-hand side does not appear, at first glance, to be cropped to the location of the leftmost closed field line, but the careful reader will note that there are, in fact, three tiny field lines that extend to the leftmost edge of the image, as shown by the arrow.

Using this method with this particular coronal field extrapolation, we are left with the unfortunate fact that the presence of these three small field lines greatly change the size of the area of synthetic and observed emissions that are compared—arguably including a large area of emission on the left-hand side that is not reliably simulated in the model. However, viable alternative methods for cropping the observed emissions are not immediately obvious. We could crop observations based on something like field line density, but because the density of field lines is a function of

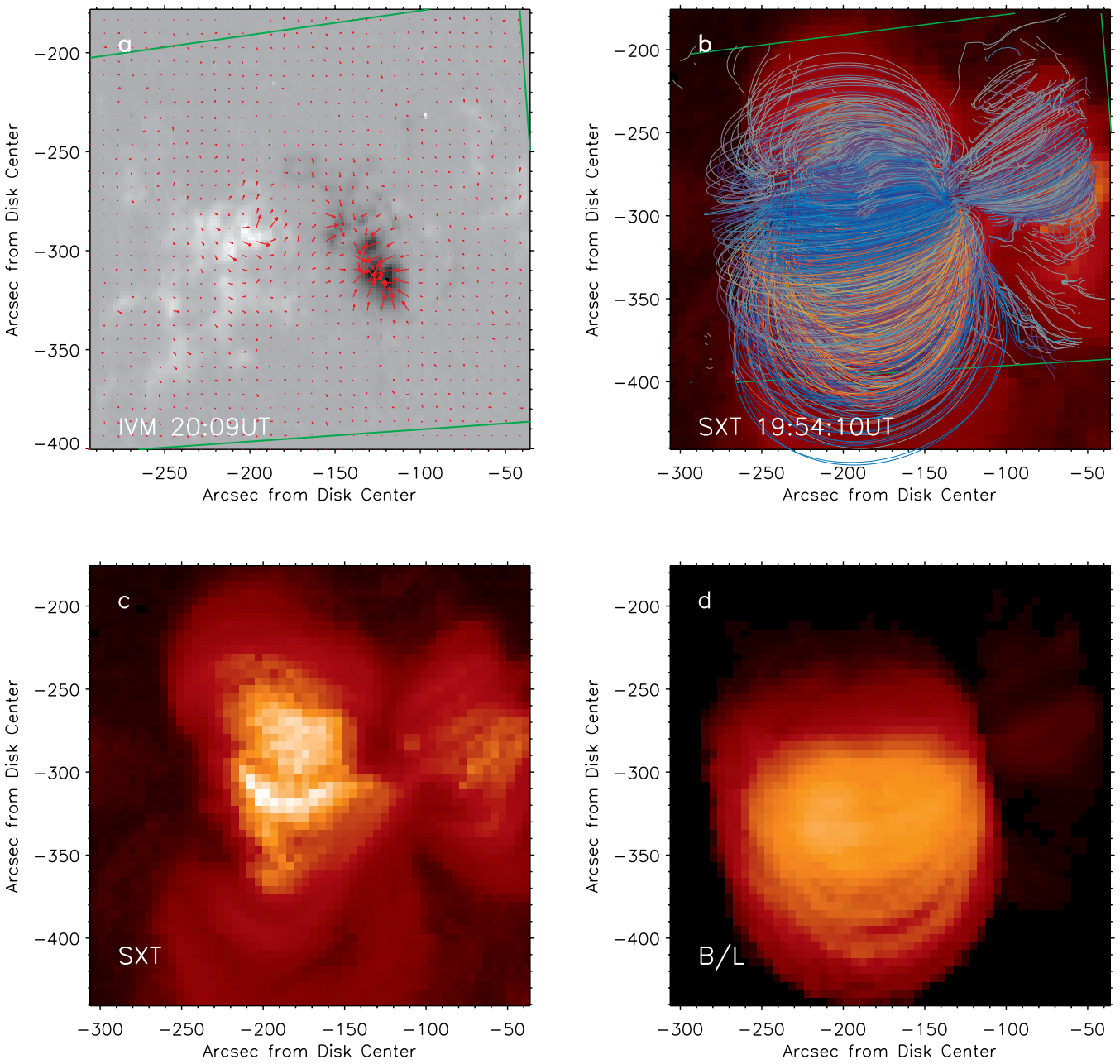

FIG. 6.—AR 9062, showing (*a*) vector magnetogram data, (*b*) field lines plotted over SXT observations, (*c*) SXT observations, and synthetic images for heating relationships (*d*) B/L, (*e*) B/L^2, (*f*) B^2/L, and (*g*) B^2/L^2. Also shown are (*h*) SXT observations in full Sun views, (*i*) all force-free field solution field lines, and (*j*) closed field lines used in synthetic image calculations. [*See the electronic edition of the Journal for a color version and panels e–j of this figure.*]

footpoint magnetic field strength, it is not clear that this would be an improvement. In other words, regions with few field lines represent a viable prediction of no emission. In fact, as discussed in Paper I, it is not clear why the observations exhibit so much emission on the left-hand side of AR 8210, given the lack of magnetic field in that region. Even beyond the border of the IVM data, there is virtually no apparent magnetic field in the MDI line-of-sight data, and the presence of emission is likely due to dynamic effects.

3.2.2. *Why Are There Field Lines that Appear to Fall Outside of the Original Magnetogram Data and/or the Force-Free Solution Box?*

No field lines fall outside of the force-free solution box. However, when field lines are displayed on the coronal emission images, they are shown in projection in the image plane. With the force-free-field solution box located normal to the surface of the Sun, some of the field lines—when projected into the image plane (normal to the line of sight of the *Yohkoh* satellite)—appear to fall outside of the bottom boundary of the force-free-field solution box, which is also shown in projection.

3.2.3. *Why Are There Field Line Footpoints that Appear to Fall Outside of the Magnetogram Data Area?*

No field lines should be anchored in regions of zero field strength. However, there are a small number of field lines that sometimes close exactly on the corner of the force-free solution box, in a location that is outside of the original magnetogram data. This appears to be an edge-effect issue with the force-free-field solution algorithm, which probably originates from discrepancies

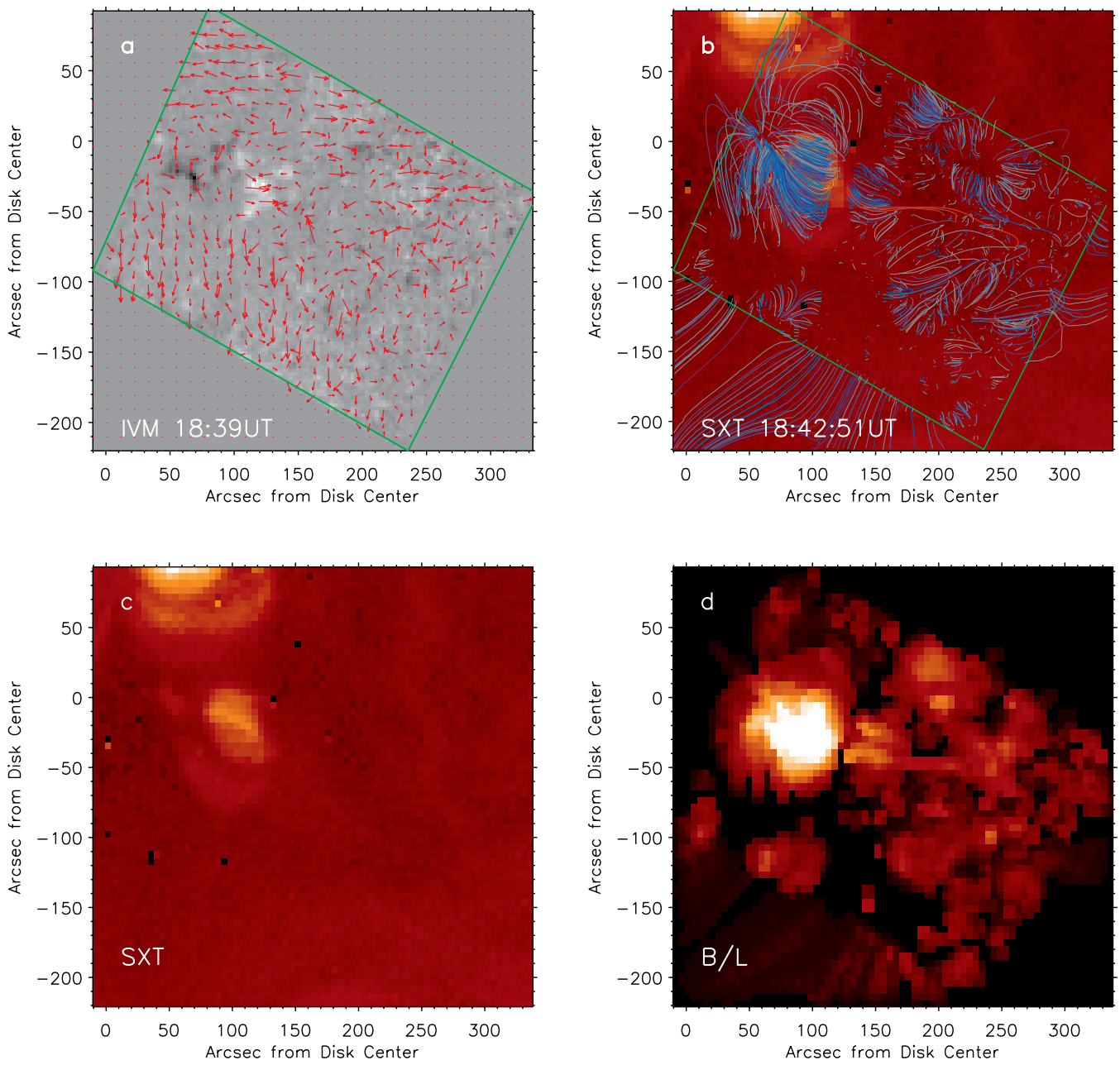

FIG. 7.—AR 9659, showing (*a*) vector magnetogram data, (*b*) field lines plotted over SXT observations, (*c*) SXT observations, and synthetic images for heating relationships (*d*) B/L, (*e*) B/L^2, (*f*) B^2/L, and (*g*) B^2/L^2. Also shown are (*h*) SXT observations in full Sun views, (*i*) all force-free field solution field lines, and (*j*) closed field lines used in synthetic image calculations. [*See the electronic edition of the Journal for a color version and panels e–j of this figure.*]

between the potential-field solution boundary imposed on the sides of the box versus the vector magnetogram data imposed on the bottom boundary of the box. This issue should probably be fixed in future versions of the code, but remains a small effect.

3.3. *3D View of Magnetic Field Lines, as in Figures 1c and 1d*

Figures 1*c* and 1*d* show field lines from the coronal magnetic field extrapolation in a 3D view. In each case, the lower left-hand corner of the magnetogram data in Figure 11*a* appears in the front bottom corner of the 3D view. Figure 1*c* shows all the field lines calculated using a minimum threshold cutoff (as described in Paper I). Figure 1*d* shows only the field lines modeled as coronal loops in the energy-balance calculations. We exclude open field lines and lines that are less than or equal to 1 pixel tall in the force-free-field solution.

3.4. *Soft X-Ray Coronal Emissions, as in Figures 2a and 2b*

Figure 2*a* shows the observed SXT image. Figure 2*b* shows a full-Sun view of the same active region. The green outline encloses the original IVM data as in Figures 1*a* and 1*b*. The white box is an outline of the observations that are compared to the synthetic images. The coronal observations in Figure 2*a* were recorded at the time stamp shown in Figure 1*b*. Those in Figure 2*b* are from the nearest time for which full-Sun observations are available. They are not necessarily plotted on the same color scale as the data shown in Figure 2*a*.

3.5. *Soft X-Ray Coronal Emissions, as in Figures 2c–2f*

Figures 2*c*–2*f* show the synthetic emission images predicted using our method for heating relationships: B/L, B/L^2, B^2/L, and B^2/L^2. The images are plotted in the same field of view as that of

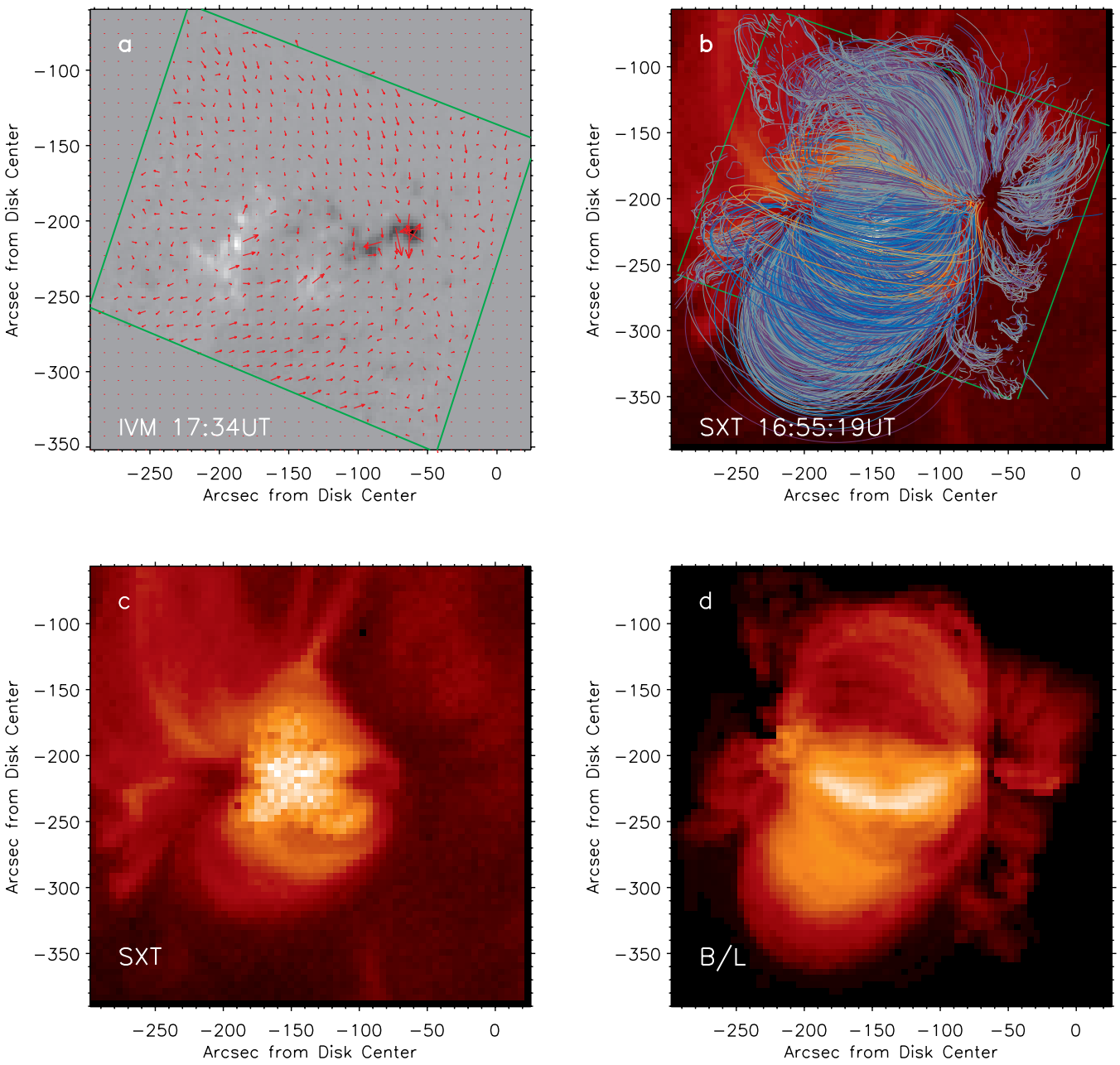

FIG. 8.—AR 9710, showing (*a*) vector magnetogram data, (*b*) field lines plotted over SXT observations, (*c*) SXT observations, and synthetic images for heating relationships (*d*) B/L, (*e*) B/L^2, (*f*) B^2/L, and (*g*) B^2/L^2. Also shown are (*h*) SXT observations in full Sun views, (*i*) all force-free field solution field lines, and (*j*) closed field lines used in synthetic image calculations. [*See the electronic edition of the Journal for a color version and panels e–j of this figure.*]

Figure 2*a*, with the same pixel sizes and locations, and the same color table and range. The images are created from magnetic data specified in the time stamp in Figure 1*a*.

3.6. *Active Region Comparisons*

We modeled emissions from 10 active regions in total, using the methods described in Paper I. Information about these active regions is given in Table 3. It gives the time, date, and size, as measured by the total unsigned magnetic flux. It tells which SXT filter was used to observe the region, as well as the secondary filter used for calculating single-filter-ratio temperatures.

Some of the regions use data from the partial field image view from SXT, which generally records data at a greater resolution than the full Sun images. We indicate whether the data used are from a partial Sun image (which may not fully overlap with the vector magnetogram data) or from full Sun images.

In some cases, the available observations were relatively dark. In these cases, we normalized to 1000 ms exposure for better image clarity. In other cases, the available observations consisted of images that were either too dark to be accurate at a normalized time exposure or so bright that bright pixels of the active region were saturated. In these cases, we take the long and short exposure pair, normalize both images, and created a time-interpolated observation, using a pixel average where nonsaturated pixels were available from both images. The time stamp listed is halfway between the times of these two observations. Normalized and/or interpolated regions are indicated in Table 3.

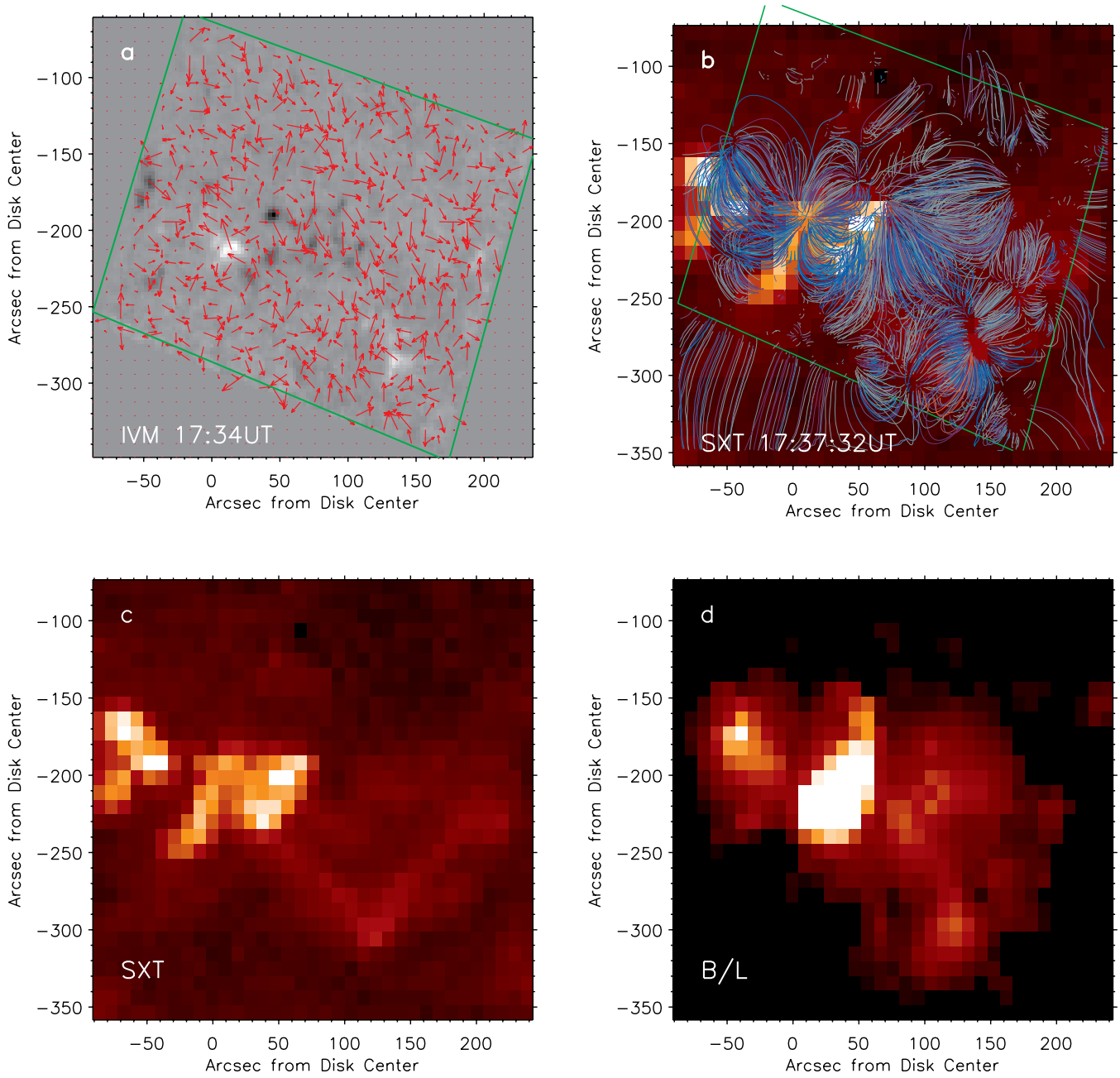

FIG. 9.—AR 9714, showing (*a*) vector magnetogram data, (*b*) field lines plotted over SXT observations, (*c*) SXT observations, and synthetic image for heating relationships (*d*) B/L, (*e*) B/L^2, (*f*) B^2/L, and (*g*) B^2/L^2. Also shown are (*h*) SXT observations in full Sun views, (*i*) all force-free field solution field lines, and (*j*) closed field lines used in synthetic image calculations. [*See the electronic edition of the Journal for a color version and panels e–j of this figure.*]

Finally, we have included some sample regions that are relatively small in magnetic field strength. For three of these, we found that the transverse magnetic field from the IVM observations was too noisy to employ in a force-free field extrapolation, so we have instead used a potential field extrapolation (Sakurai 1982). This is also indicated in Table 3.

For the latter nine active regions in the table, we present the photospheric magnetic field observations, coronal magnetic field solutions, observed SXT emissions, and synthetic emissions from the four heating parameterizations in Figures 1–10. For each of the 10 regions, we present in Table 2 quantitative comparisons between observations and predictions from each heating parameterization. See Paper I for a discussion of the calculation of these values, including the weighted rms relative error σ of the emission and temperature and emission measure values.

3.6.1. *Summary*

Table 2 summarizes the results from all 10 active regions. With respect to image prediction accuracy, the statistical comparisons show that the four heating parameterizations rank as follows: (1) B/L, (2) B^2/L, (3) B/L^2, and (4) B^2/L^2. This agrees with our qualitative assessment. In general we find that visually, the synthetic images with heating that scales as $1/L$ do a better job of reproducing the observed emissions than the images with heating that scales as $1/L^2$.

There is a significant difference between the end members of this ranking, with B/L scaling giving predicted pixel intensities

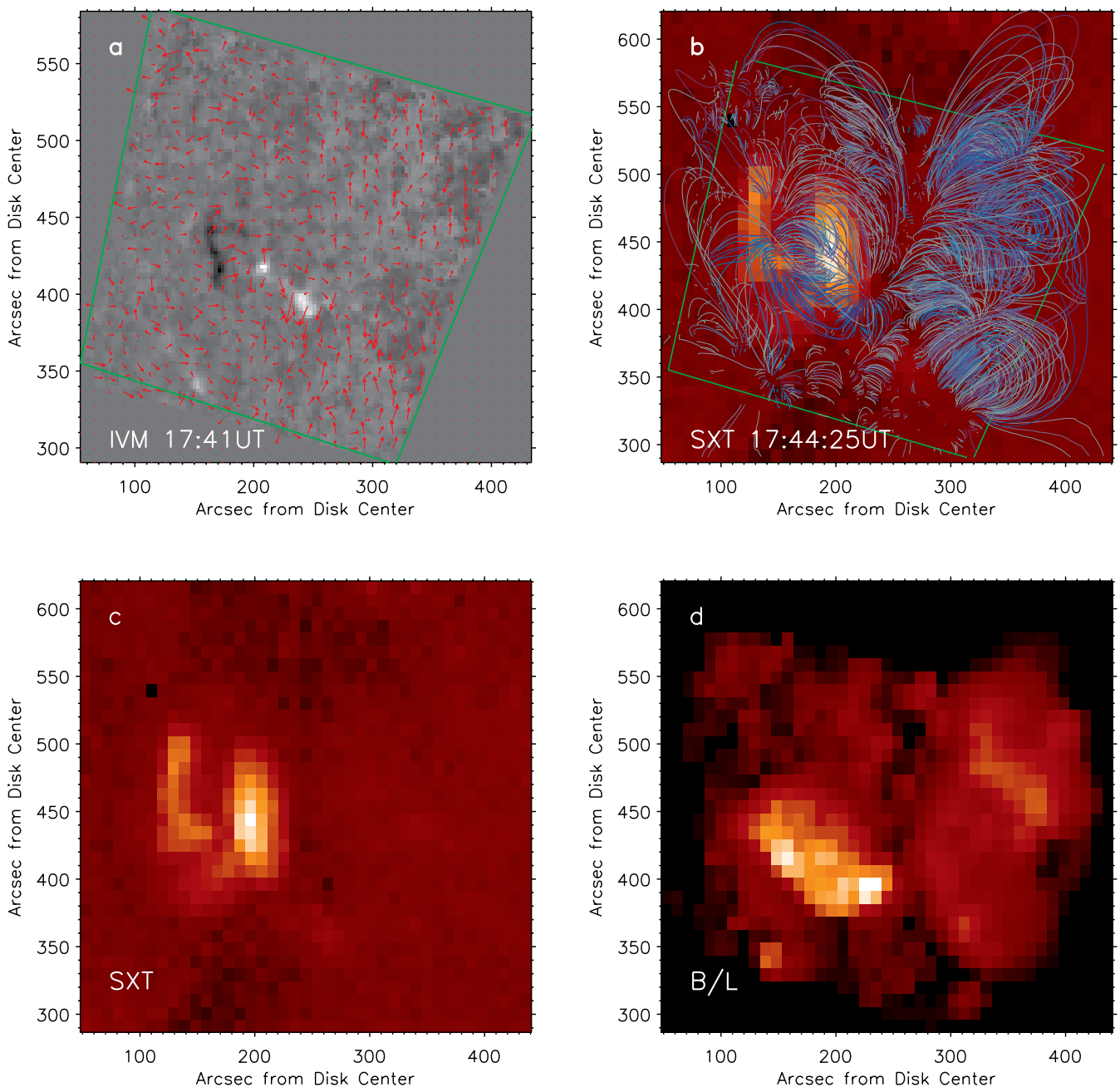

FIG. 10.—AR 9731, showing (*a*) vector magnetogram data, (*b*) field lines plotted over SXT observations, (*c*) SXT observations, and synthetic images for heating relationships (*d*) B/L, (*e*) B/L^2, (*f*) B^2/L, and (*g*) B^2/L^2. Also shown are (*h*) SXT observations in full Sun views. (*i*) all force-free field solution field lines, and (*j*) closed field lines used in synthetic image calculations. [*See the electronic edition of the Journal for a color version and panels e–j of this figure.*]

with typical errors of about 200%, while B^2/L^2 gives pixel intensity errors on the order of about 1650%.

Surprisingly, when considering all 10 active regions as a whole, all of the scaling relationships do a reasonably good job of predicting the single-temperature filter ratio values. For each scaling relationship, one can compute the mean temperature error for the sample of 10 active regions, by averaging the difference between the measured and computed active region temperatures. This quantity indicates whether a particular scaling relationship results in a systematic bias of the computed temperature with respect to the measured values. As shown in Table 3, each of the scaling relationships results in a mean bias of less than ~20% in magnitude, with B/L^2 heating underestimating temperature, and the remaining heating relationships overestimating it. For individual active regions, temperatures inferred from the models can be systematically lower than the observed value (e.g., AR 8210, where model values range from 20%–40% lower) or systematically higher (e.g., AR 9026). Therefore, while the pixel intensity comparisons strongly favor the B/L relationship, there is no strong preference for any particular heating model from agreement with filter ratio temperatures.

4. DISCUSSION AND CONCLUSIONS

We have presented results from forward-modeling studies of 10 different active regions. We have calculated the expected soft X-ray coronal emissions for each of these regions, given vector magnetic data from the region at the solar photosphere. To simulate different proposed coronal heating mechanisms, we have

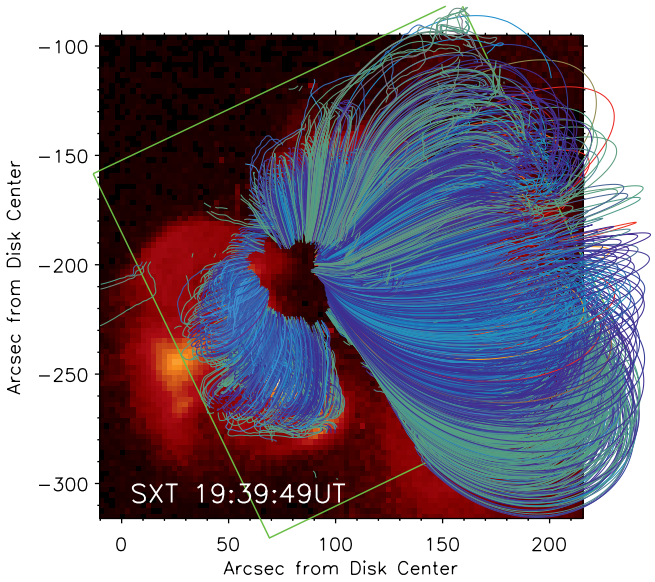

FIG. 11.—AR 8210, showing field lines plotted over SXT observations. (See Paper I for synthetic images.) [*See the electronic edition of the Journal for a color version of this figure.*]

adopted four different parameterizations of the volumetric heat flux deposited in the corona, based on properties of the magnetic field: heating that scales as B/L, B/L^2, B^2/L, and B^2/L^2.

4.1. *Accuracy of Forward Modeling*

We find that the forward models generally do a poor job of representing the observations. Even for the best heating relationship, pixel intensities typically disagree with observed values by 200%. We note, however, that the reported error values tend to overestimate the prediction error of our basic technique, due to the frequent and substantial lack of complete overlap between the simulation volume and the coronal volume that contributes to the observed X-ray images. This means that the weighted rms relative error values include comparisons between pixels for which there are no model data, or where the integrated line-of-sight path does not penetrate through the full height of the emission simulations. These effects would be eliminated for magnetogram data and coronal observations located at disk center and with zero solar p-angle—the only case where the simulated and observed coronal volumes overlap completely.

In Paper I, we considered the effects of different forward-modeling assumptions on the predicted intensities, including potential vs. force-free fields, magnetic field line representation, filling factors, distribution of loop energy deposition, and elemental abundances. Varying each of these assumptions resulted in little improvement in our model's ability to reproduce the observations. Examination of the 10 regions presented in this paper suggest that a significant factor in our lack of success in reproducing the observed emissions can be attributed discrepancies in the coronal magnetic field solution compared to the Sun's actual field distribution.

In some cases, the restricted field of view of observations results in artifacts and edge effects, such as the "open" field lines that probably extend only a short distance outside of the simulation box, but must nevertheless be discarded due to incomplete magnetic information. Clearly, this situation would be greatly improved by a wider field of view. The availability of full-Sun vector magnetic data is expected soon from SOLIS. However, even with the availability of such data, the computational time necessary to achieve nonlinear force-free field extrapolations for a wider field of view is daunting. Nevertheless, even employing the same size model volume as we do here, there would be much to gain from the availability of full-Sun data, such as (1) the ability to vary the exact window of view to include all of the nearby magnetic flux, and (2) the ability to include the "corners" of magnetogram data that are currently set to zero due to solar p-angle differences between the coronal images and the magnetogram data. The latter improvement would increase the overlap between the simulated volume and the observed volume discussed above, although aspects of the problem would remain due to projection effects of a region located away from disk center with a simulation cube normal to the solar surface. The former consideration would help to improve the longitudinal magnetic flux balance within the magnetogram field of view, resulting in a greater percentage of closed flux regions on the Sun simulated in our model.

There are a number of cases where the coronal magnetic field does not match the observed loop morphology well, even when we do appear to have an appropriate field of view and relatively

TABLE 2
RELATIVE ERRORS FOR ALL REGIONS

ACTIVE REGION	Φ_{tot} (Mx)	σ				TOTAL RELATIVE ERROR			
		B/L	B/L^2	B^2/L	B^2/L^2	B/L	B/L^2	B^2/L	B^2/L^2
AR 8210	2.7×10^{22}	2.3	2.8	2.1	4.1	−0.2	−0.4	−0.2	−0.3
AR 8651	6.1×10^{22}	1.1	11.0	1.2	16.7	−0.2	−0.3	−0.2	−0.3
AR 8891	6.1×10^{22}	1.1	2.2	1.3	3.8	−0.3	−0.4	−0.3	−0.4
AR 9017	3.2×10^{22}	2.6	36.9	3.5	49.5	0.2	−0.1	0.2	−0.0
AR 9026	5.5×10^{22}	2.4	10.1	7.0	17.2	0.9	0.6	0.9	0.9
AR 9062	2.4×10^{22}	2.4	7.0	1.4	16.6	−0.3	−0.5	−0.3	−0.4
AR 9659	8.6×10^{21}	3.1	4.8	21.3	24.2	−0.1	−0.3	−0.0	−0.1
AR 9710	3.4×10^{22}	1.3	3.7	1.8	5.4	0.5	0.0	0.4	0.0
AR 9714	1.2×10^{22}	1.5	4.0	5.8	9.1	1.4	0.8	1.6	1.3
AR 9731	2.4×10^{22}	2.3	4.1	17.2	18.3	...	...	...	...
Mean Values		2.0	8.7	6.3	16.5	0.2	−0.07	0.2	0.09
Unsigned Means		...	...	...	...	0.5	0.4	0.5	0.4

NOTES.—For each active region, gives total unsigned magnetic flux Φ_{tot}, weighted relative rms error in pixel intensity, σ, for synthetic emission images using each heating parameterization, and the relative error in temperature, $T_{relerror}$, for each heating parameterization. Mean of absolute values of σ and $T_{relerror}$ appear at the end, as well as unsigned mean (mean of absolute values) for $T_{relerror}$.

TABLE 3
Active Regions Studied

Active Region	Φ_{tot} (Mx)	Date	Time (UT)	Filter 1	Filter 2	Full/ Partial?	Normal?	Interpretation?	Magnetic Field
AR 8210.....	2.7×10^{22}	1998 May 1	19:39:49	AlMg	Al.1	Partial	N	N	fff
AR 8651.....	6.1×10^{22}	1999 Aug 2	17:00:50	Al.1	AlMg	Partial	Y	N	fff
AR 8891.....	6.1×10^{22}	2000 Mar 1	20:22:53	AlMg	Al.1	Partial	N	N	fff
AR 9017.....	3.2×10^{22}	2000 Mar 1	17:56:58	AlMg	Mg3	Full	Y	N	fff
AR 9026.....	5.5×10^{22}	2000 Jun 5	17:11:35	AlMg	Al.1	Partial	N	N	fff
AR 9062.....	2.4×10^{22}	2000 Jun 30	19:54:10	Al.1	AlMg	Full	Y	Y	fff
AR 9659.....	8.6×10^{21}	2001 Oct 12	18:42:51	AlMg	Al.1	Full	N	N	Pot
AR 9710.....	3.4×10^{22}	2001 Nov 21	16:55:19	Al.1	AlMg	Full	Y	Y	fff
AR 9714.....	1.2×10^{22}	2001 Nov 25	17:37:32	AlMg	Al.1	Full	N	N	Pot
AR 9731.....	2.4×10^{22}	2001 Dec 10	17:44:25	AlMg	...	Full	N	N	Pot

Notes.—For each active region, gives the total unsigned magnetic flux Φ_{tot}, date and time of SXT observations, filter used for observations and reconstructed emissions, and secondary filter used to determine temperature. Also indicates whether the observed image was interpolated between two observation times, normalized to an exposure time of 1000 ms, and whether a potential (pot) or force free (fff) coronal magnetic model field was used.

acceptable flux balance, such as the cases of AR 8210, AR 9026, and AR 8651. The force-free field solution is state-of-the-art–one of the most accurate force-free field techniques available today, according to the comparisons of Schrijver et al. (2005, 2006), yet the accuracy of the coronal magnetic field solution remains a major stumbling block. This may be due to instances where the coronal field is changing dynamically and may not be in a force-free equilibrium, as we suspect for AR 8210 (see discussion in Paper I). In other cases, the region may be in a force-free state, but one affected by previous evolutionary history, including reconnection and flux emergence/submergence, about which we have no information from a single magnetogram. A 3D MHD model is probably needed if one wants to account for history-dependent magnetic topology. The matter is further complicated by the fact that the high-β photosphere, where the magnetic field is measured, is not expected to be in a force-free state and by the fact that the force-minimization algorithm yields a solution that is not fully force-free. We conclude that there is much room for improvement and development in coronal field extrapolation techniques.

A second major factor impairing the accuracy of the coronal emission predictions is our steady-state equilibrium approximation. The steady-state model's temperature and emission measure predictions imply that many loops are probably heated intermittently, as discussed in Paper I, placing them outside the realm of the steady-state approximations. Relaxing this approximation would certainly change the simulation's temperature and emission measure values and emission predictions.

A third issue we face in these simulations is the transition from 1D to 3D emission estimates. As discussed in § 1, a 1D simulation is necessary at this point to resolve the transition region. However, the 1D technique results in an undersampling of the coronal volume, particularly at higher altitudes. No interpolation technique that we have tested can overcome this defect. Rather than adopt a technique that spawns artifacts at these undersampled regions, we chose instead a first-order schema that assigns a value of zero to voxels located more than 1 voxel width away from a coronal loop (see Paper I). However, this has unintended effects on our emissions predictions. The interpolation resolution is determined by the SXT pixel resolution, but the estimate of total emissions can change when the resolution is changed, due to the larger volume with points that lie more than 1 voxel away from simulated coronal loops. In the example of AR 8210, doubling the resolution results in a change of about 20% in total emissions. The effect levels off as resolution is increased further. Because the constant of proportionality in the heating relationship is chosen to match total emissions to observed emissions, this can have a small effect on emission morphology and temperature, and a somewhat larger effect on emission measure. (The relationship between proportionality constant and emission measure for each heating law is shown in Paper I.) A more accurate or appropriate interpolation schema is needed for 1D calculations such as ours, although the best solution would be a fully 3D calculation.

It is difficult to assess the relative importance of these three factors, but we believe addressing these three shortcomings offers the best opportunity for improving coronal emissions predictions. Other improvements could stem from numerous other sources, including our chosen heating parameterizations—perhaps the true coronal heating mechanism is represented by a scaling relationship other than the four we have chosen. We speculate that coronal magnetic field extrapolation inaccuracies remain the biggest impediment to accurate coronal modeling. Circumstantial evidence for this view may be found from examination of Figure 5 and the corresponding figures for other active regions. These examples show marked discrepancies between emission morphology and field-line morphology. Such failings will not be overcome with better heating parameterizations, improved loop models (with or without dynamics), interpolation advancements, or even from 3D simulations such as that of Mok et al. (2005), which begin with a coronal extrapolation.

4.2. *Coronal Heating Implications*

In spite of substantial inaccuracies of all of the predictions, it is clear that our basic technique remains promising, as shown by the dramatic differences between the predictions of different heating parameterizations. Keeping in mind the model's shortcomings, we are able to draw some conclusions regarding coronal heating.

We find that a volumetric coronal heating rate which scales as $\bar{B}/L$ is the best predictor of coronal emission morphologies and nearly the best predictor of temperatures measured using filter-ratio techniques. Overall, we find that the two relationships with $1/L$ scaling predict temperatures and synthetic emissions much better than relationships with $1/L^2$ scaling. Indeed, for the two active regions we have simulated most accurately (AR 8891 and AR 8651), there is little difference between the $\bar{B}/L$ and $\bar{B}^2/L$ scalings.

Figure 12 shows the parameter space explored by our simulations compared to the parameter space of B and L scalings from the 22 heating theories discussed in MDK. Each theory is considered in

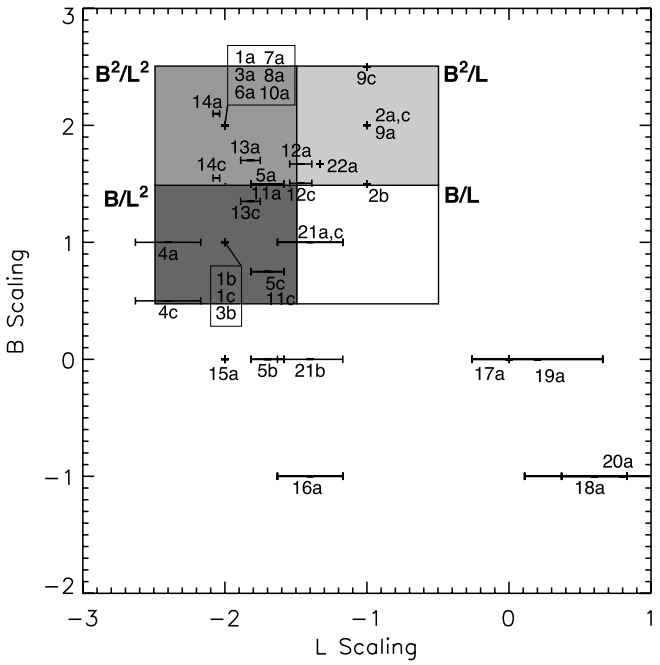

FIG. 12.—Parameter space of B and L scaling for our simulations vs. 22 coronal heating theories from MDK. Heating mechanisms are labeled by the model number and case letter listed in Table 1. Horizontal bars show the range in L scaling for different values of ϵ. Simulated parameter ranges are shown with shaded boxes, with shading that indicates ranking of parameterizations from our simulations (lighter shading within these boxes indicates better fit).

the three cases for B scaling shown in Table 1, corresponding to different assumptions about the nature of the R and V variables. Each of these cases also has a range of possible L scalings depending on assumptions for how ρ scales with L.

We have evaluated four parameterizations with integer scaling exponents. We represent these four models using boxes with a width of unity in Figure 12. Increased shading in these boxes represents poorer synthetic emission image results. We note that if B and L scaling exponents from Table 1 are rounded to the nearest integer, the B and L parameter space range encompasses all of the theories in the table except for those which predict a heating that scales either inversely or not at all with the magnetic field.

Only one of the proposed heating mechanisms, model 21 in cases (a) and (c), falls within the box representing B/L scaling. This is the "current layers" model first introduced by van Ballegooijen (1986), where energy pumped into the field through photospheric footpoint motions undergoes a kinematic cascade to scales small enough for Ohmic dissipation to be significant. The scaling from this theory is consistent with our results only in the "AC" limit, where footpoint motions are rapid compared with the end-to-end Alfvén travel time of the coronal loops.

The range of possible L values is a result of the different options for ϵ, the exponent in the relationship between mass density ρ and loop length L, discussed in § 2. We find in our simulations that loops heated with different parameterized heating terms exhibit different power-law relationships with different values of ϵ. For B/L heating, we find a value of $\epsilon = -0.36 \pm -0.03$, by examining scatter plots of the individual loop solutions. This corresponds to the upper limit in the range of L scaling, giving a scaling of $BL^{-1.17}$ for model 21. Thus, the value of ϵ derived from correlating density with loop length for the simulated loops is relatively self-consistent with the assumed heating scale relationship. This value is also well within the MDK 90% confidence range of $\epsilon \in [-1.55, 0.20]$.

One other proposed heating mechanism, model 2 in case (b), lies directly on the boundary between the two best heating parameterizations favored by our model. This model is a variation on the "critical angle" theory postulated by Parker (1988), in which magnetic footpoints do a random walk about the photosphere, causing the field to become entangled. However, in the case (b) formulation of this theory, the velocity is interpreted as a twist-type velocity, and flux tubes become twisted rather than braided. In this version, the critical angle θ at which heating occurs represents the angle between twisted field lines at the outer edges of adjacent tubes. Model 2(b) does not scale with ρ, so we need not need check for self-consistency in ϵ values.

The bulk of the theories in Figure 12 fall in the realm of the two poorest heating parameterizations, those which scale with $1/L^2$. A large number of heating theories fall in the domain of B^2/L^2 heating, the theory which exhibits the worst predictions of both emission morphology and temperature. In our estimation, not one of the synthetic emission images created with this scaling relationship looks like the observed emissions image, and the misfit statistics support this statement. Even with improved magnetic field morphologies, it is not likely that these synthetic images would improve. This is strong circumstantial evidence against the heating mechanisms that fall within this domain.

Although the B/L^2 parameterization performs poorly overall, the evidence against theories in this region is weaker, particularly since the B/L^2 theory yields some synthetic emission images that appear visually similar to the observations in at least a few cases, most notably AR 8210. Nevertheless, if we were to rule out all $1/L^2$ theories (corresponding to the left half of our simulated parameter space in Fig. 12), we would be left with only five viable theories of the original 22. These include models 2, 9, 12, 21, and 22.

Our results are consistent with the observed relationship of Fisher et al. (1998) and Pevtsov et al. (2003) that total emission from active regions scales nearly linearly with magnetic flux. Our results differ, however, from the findings of Schrijver et al. (2004), who find for full-Sun visualizations that the heat flux density flowing to the corona, F_H, scales as B/L. While our preferred scalings appear identical ("B/L"), we are actually referring to different quantities. Their F_H, with units of ergs cm^{-2} s^{-1}, differs from our volumetric heating term E_H by a factor with a unit of length. For a coronal loop with constant cross sectional area, this factor would be the loop length, L, and their finding of $F_H \propto B/L$ would correspond to a volumetric heating $E_H \propto B/L^2$, except that they use the chromospheric footpoint magnetic field strength in their formulation, while we use the magnetic field strength averaged over the length of the loop, $\int B\,ds / \int ds$.

We have already noted a number of the differences between our model and that of Schrijver et al. (2004), including loop simulations with steady state flows, allowing for continuous temperature and density profiles at the loop apex (vs. a static equilibrium loop model), and a nonlinear quasi-force-free extrapolation for the coronal magnetic field. We also use average loop field strength in the heating parameterization as described above, as opposed to footpoint field strength. An additional difference is our field-line representation of the corona; we have more field lines where there is stronger field, while Schrijver et al. (2004) choose field lines distributed evenly across the solar surface.

Our investigations in Paper I showed that adopting the Schrijver et al. choices for the coronal magnetic field, such as a potential field solution or field lines distributed evenly on the photosphere, does not greatly affect the synthetic image reconstructions. Many of the individual loop simulations do not differ greatly from a static solution, as the example in Paper I shows, although the effect may be

more substantial for emissions over the entire active region. They also employ a scale height that results in a small tendency toward footpoint heating. A final difference is that we interpolate to a 3D grid, while they show emissions along individual loops.

The source of the discrepancy between our results and those of Schrijver et al. (2004) is not clear and may require further investigation. Because the poor fit of the $1/L^2$ parameterizations in our model largely stems from very short loops, we speculate that the discrepancy may be due to the presence of more short loops in our simulations, perhaps due to higher resolution calculations of the magnetic field. On the other hand, Warren & Winebarger (2006) suggest that if the average coronal field strength B scales with the footpoint field strength B_0 and loop length L as $B \sim B_0/L$, that the Schrijver et al. (2004) results may be consistent with a volumetric heating rate that scales as B/L. This speculation, while plausible, remains to be demonstrated. Alternatively, the discrepancy may suggest that a different heating mechanism dominates in the quiet Sun or coronal hole regions than in active regions. However, our results do confirm the Schrijver et al. (2004) finding that a heating that scales as B^2 tends to result in too much contrast between strong and weak field regions. Although they find this to be true over the whole Sun, we find the same tendency within individual active regions.

A particularly relevant effort to our own investigation is that of Warren & Winebarger (2006), who used a similar approach to ours to study heating in a sample of 26 active regions observed by *SOHO*'s MDI and EIT instruments, and by the *Yohkoh* SXT telescope. The major differences between their models and ours are that they used line-of-sight magnetograms from MDI to construct potential field models, rather than using vector magnetograms to construct nonlinear force-free-field models; they used the field-line solutions themselves to compute emission intensities, rather than interpolating to a 3D grid (this is also the technique used by Schrijver et al. 2004); and they used simplified static models assuming no cross sectional area variation to compute the thermodynamic quantities along each field line, instead of accounting for area variation and steady flows along the loops that accompany asymmetries in field strength along loops. The Warren & Winebarger (2006) heating model is essentially identical to the one employed in the present study. From their sample of active regions, they conclude that a volumetric heating rate that scales as B/L fits the observations better than the other heating parameterizations—a conclusion in accord with ours, reached in this paper. The fact that two independent investigations of heating in active regions, using somewhat different modeling details, reach the same conclusion, is encouraging. Warren & Winebarger (2007) also begin to extend the approach using dynamic loop models. This preliminary effort with a single active region points toward consistency with both our results and those of Warren & Winebarger (2006).

The forward-modeling effort described here represents an important step in understanding the physics of the solar corona, particularly with regard to coronal heating mechanisms. Only recently has it become possible to accomplish a modeling effort such as this, simulating the emissions from thousands of loops across an entire active region. However, it still looms as a crucial task to determine the sources of discrepancy between the synthetic images and the observations, as well as between the variety of studies published thus far. With continuing improvements in computing resources, such developments should be rapid. Although projected improvements in instrumentation and observational techniques also promise great advances in our understanding of the corona, for the foreseeable future they will not achieve the resolution required to directly observe heating mechanisms at work. Thus, through the study conducted here and those which will evolve from it, forward-modeling efforts of this type will form a crucial part of the ultimate discovery of the true solar coronal heating mechanism.

L. L. L. appreciates funding from a NASA Graduate Student Research Program Fellowship and DoD MURI grant "Understanding Magnetic Eruptions on the Sun and Their Interplanetary Consequences." G. H. F. was supported by the same DoD MURI grant, and by NASA through the Heliophysics Supporting Research and Technology Program (award NNG05GF65G-3/08), and through the Theory Program (award NNG05G144G-04/08). J. M. M. was supported by a grant from the Solar, Heliospheric and INterplanetary Environment (SHINE) group. We thank W. Abbett, B. Welsch, and D. Bercik for many helpful discussions.

REFERENCES

Aly, J. J., & Amari, T. 1997, A&A, 319, 699
Aschwanden, M. J. 2004, Physics of the Solar Corona: An Introduction (Chichester: Springer Praxis)
Aschwanden, M. J., & Schrijver, C. J. 2002, ApJS, 142, 269
Berger, M. A. 1991, A&A, 252, 369
———. 1993, Phys. Rev. Lett., 70, 705
Browning, P. K., & Priest, E. R. 1986, A&A, 159, 129
Démoulin, P., van Driel-Gesztelyi, L., Mandrini, C. H., Klimchuk, J. A., & Harra, L. 2003, ApJ, 586, 592
Dmitruk, P., & Gomez, D. O. 1997, ApJ, 484, L83
Einaudi, G., Velli, M., Politano, H., & Pouquet, A. 1996, ApJ, 457, L113
Falconer, D. A. 1997, Sol. Phys., 176, 123
Fisher, G. H., Longcope, D. W., Metcalf, T. R., & Pevtsov, A. A. 1998, ApJ, 508, 885
Foley, C. R., Patsourakos, S., Culhane, J. L., & MacKay, D. 2002, A&A, 381, 1049
Galsgaard, K., & Nordlund, A. 1996, J. Geophys. Res., 101, 13445
———. 1997, J. Geophys. Res., 102, 219
Golub, L., Maxson, C., Rosner, R., Vaiana, G. S., & Serio, S. 1980, ApJ, 238, 343
Gomez, D. O. 1990, Fundam. Cosmic Phys., 14, 131
Halberstadt, G., & Goedbloed, J. P. 1995, A&A, 301, 559
Hendrix, D. L., van Hoven, G., Mikic, Z., & Schnack, D. D. 1996, ApJ, 470, 1192
Heyvaerts, J., & Priest, E. R. 1984, A&A, 137, 63
———. 1992, ApJ, 390, 297
Hollweg, J. V. 1985, in Advances in Space Plasma Phys., ed. B. Buti (Singapore: World Scientific), 77
Inverarity, G. W., & Priest, E. R. 1995a, A&A, 296, 395
———. 1995b, A&A, 302, 567
Inverarity, G. W., Priest, E. R., & Heyvaerts, J. 1995, A&A, 293, 913
Klimchuk, J. A. 2006, Sol. Phys., 234, 41
Klimchuk, J. A., Antiochos, S. K., & Norton, D. 2000, ApJ, 542, 504
Klimchuk, J. A., & Cargill, P. J. 2001, ApJ, 553, 440
Klimchuk, J. A., Lemen, J. R., Feldman, U., Tsuneta, S., & Uchida, Y. 1992, PASJ, 44, L181
Klimchuk, J. A., & Porter, L. J. 1995, Nature, 377, 131
Lopez Fuentes, M. C., Klimchuk, J. A., & Demoulin, P. 2006, ApJ, 639, 459
Lundquist, L. L., Fisher, G. H., & McTiernan, J. M. 2008, ApJS, 179, 509 (Paper I)
Lundquist, L. L., Fisher, G. H., McTiernan, J. M., & Régnier, S. 2004, in Coronal Heating, ed. R. W. Walsh et al. (ESA SP-575; Noordwijk: ESA), 306
Mandrini, C. H., Démoulin, P., & Klimchuk, J. A. 2000, ApJ, 530, 999 (MDK)
Martens, P. C. H., Cirtain, J. W., & Schmelz, J. T. 2002, ApJ, 577, L115
Milano, L. J., Gomez, D. O., & Martens, P. C. H. 1997, ApJ, 490, 442
Mok, Y., Mikic, Z., Lionello, R., & Linker, J. A. 2005, ApJ, 621, 1098
Narain, U., & Ulmschneider, P. 1996, Space Sci. Rev., 75, 453
Ofman, L., Davila, J. M., & Shimizu, T. 1996, ApJ, 459, L39
Ofman, L., Davila, J. M., & Steinolfson, R. S. 1995, ApJ, 444, 471
Parker, E. N. 1983, ApJ, 264, 642
———. 1988, ApJ, 330, 474
Pevtsov, A. A., Fisher, G. H., Acton, L. W., Longcope, D. W., Johns-Krull, C. M., Kankelborg, C. C., & Metcalf, T. R. 2003, ApJ, 598, 1387

Porter, L. J., & Klimchuk, J. A. 1995, ApJ, 454, 499
Reale, F., & Peres, G. 2000, ApJ, 528, L45
Ruderman, M. S., Berghmans, D., Goossens, M., & Poedts, S. 1997, A&A, 320, 305
Sakurai, T. 1982, Sol. Phys., 76, 301
Schmelz, J. T., Beene, J. E., Nasraoui, K., Blevins, H. T., Martens, P. C. H., & Cirtain, J. W. 2003, ApJ, 599, 604
Schrijver, C. J., & Aschwanden, M. J. 2002, ApJ, 566, 1147
Schrijver, C. J., Derosa, M. L., & Metcalf, T. 2005, AGU Spring Meeting, Abst. SH31A-05
Schrijver, C. J., et al., 2006, Sol. Phys., 235, 161
Schrijver, C. J., Sandman, A. W., Aschwanden, M. J., & DeRosa, M. L. 2004, ApJ, 615, 512
Sturrock, P. A., & Uchida, Y. 1981, ApJ, 246, 331
van Ballegooijen, A. A. 1986, ApJ, 311, 1001
Vekstein, G. E., Priest, E. R., & Steele, C. D. C. 1993, ApJ, 417, 781
Walsh, R. W., & Ireland, J. 2003, A&A Rev., 12, 1
Warren, H. P., & Winebarger, A. R. 2006, ApJ, 645, 711
———. 2007, ApJ, 666, 1245
Watko, J. A., & Klimchuk, J. A. 2000, Sol. Phys., 193, 77
Weber, M. A., Schmelz, J. T., DeLuca, E. E., & Roames, J. K. 2005, ApJ, 635, L101
Withbroe, G. L., & Noyes, R. W. 1977, ARA&A, 15, 363
Yashiro, S., & Shibata, K. 2001, ApJ, 550, L113
Zirker, J. B. 1993, Sol. Phys., 148, 43